Spectrum of Engineering Sciences
ISSN (e) 3007-3138 (p) 3007-312X Volume 4, Issue 2, 2026

BIOMECHANICAL STRESS ANALYSIS OF TIBIAL BONE PLATE FIXATION SYSTEMS UNDER DIFFERENT LOAD SCENARIOS

Areej Ateeque[*1], Sehreen Moorat[2], Sasuee Khatoon[3], Natasha Mukhtiar[4]

[*1,2]*Institute of Biomedical Engineering and Technology, Liaquat, University of Medical and Health Sciences, Jamshoro, Pakistan*
[3]*Liaquat University of Medical and Health Sciences, Jamshoro, Pakistan*
[4]*Institute of Biomedical Engineering and Technology, Liaquat, University of Medical and Health Sciences, Jamshoro, Pakistan*

[*1]areejateeque05@gmail.com, [2]sehreen.moorat@lumhs.edu.pk, [3]sasuee.khatoon@lumhs.edu.pk, [4]natasha.mukhtiar@lumhs.edu.pk

DOI: https://doi.org/10.5281/zenodo.18536785

Keywords
Tibial fractures, COMSOL, Deformation, Stress distribution, Metal alloys, Torsional moment, Bending moment, Extension force, Compression force.

Article History
Received: 10 December 2025
Accepted: 25 January 2026
Published: 09 February 2026

Corresponding Author: *
Areej Ateeque

Abstract

Tibia fractures in humans are typically the result of accidents with vehicles or falls. Biomedical implants are often necessary for patients of such accidents to help in the healing process. By improving the physiological state, bone plates and other biomedical implants enable elderly individuals and car accident patients to enjoy normal lives. When a human bone is exposed to an extreme load that is above its maximum capacity, it frequently fractures. Bone healing occurs in two basic ways: primary bone healing and Secondary bone healing. This research aims to investigate the stress distribution on bone and plate under various physiological conditions, including bending, torsion, compression, and extension, using two distinct materials for the plate and screws. A 3D model's mechanical strength may be seen by simulating various mechanical tests, such as von Mises stress and maximal first principal stress, using FEA software like COMSOL. Create a three-dimensional model of the screws, metal plate, and tibia bone, then allocate the materials to the model. After applying certain load and boundary conditions, the model is then meshed and analyzed. The results of the COMSOL Multiphysics simulation indicate that modest deformation and stress levels are caused by bending, torsion, compression, and extension, but combined loads cause high deformation and stress levels. The maximum deformation in the combined load condition is 25.299 mm in Ti alloy material, whereas the smallest deformation in compression is 0.1500 mm in the same material. In stainless steel, the lowest von Mises stress is displayed in compression at 3.5606x107 N/m², while the highest is displayed in combined load at 9.8428x108 N/m². Results showed that the titanium alloy Ti-6Al-4V exhibited better performance under combination loading compared to stainless steel, with lower stress concentrations and deformation. This information can be valuable for designing implants or structures that will be subjected to various loading conditions in real-world applications.

1 INTRODUCTION

Bone is a naturally occurring tissue made up of calcium crystals in the inorganic phase, which is constituted of 10% water, 60% mineral, and 30% matrix[1], [2]. Bone tissues come in two varieties: cortical bone, which has an elastic modulus between 17×10^9 and 20×10^9 Pa, and cancellous bone, which has an elastic modulus between 5×10^7 and 1×10^8 Pa. The tibia, which bears the majority of the body weight in the lower limbs, is one of the most often broken long bones in the body[3], [4]. It is therefore known to be one of the most fractured long bones in the human body, contributing to up to 37% of lower limb failure annually, which are frequently caused by car crashes, falls, or injuries sustained during sports [5]. Biomedical implants are often necessary for patients of such accidents to help in the healing process. By improving the physiological state, bone plates and other biomedical implants enable elderly individuals and car accident patients to enjoy normal lives. When a human bone is exposed to an extreme stress that is above its maximum capacity, it frequently fractures [6]. Bone healing occurs in two basic ways. Absolute stability constructions that reach a structural stress of less than 2% are responsible for primary bone healing [7]. Haversian remodeling is the process by which intramembranous bone repair takes place. Secondary bone healing, on the other hand, happens with non-rigid fixation techniques, including braces, external fixation, bone plates, intramedullary nailing, etc. The structural stress achieved by these fixing techniques ranges from 2 to 10% and endochondral bone repair is how it happens[8]. Depending on the stability of the whole structure, a combo of primary and secondary mechanisms may be involved in bone healing. The majority of the bone plates used here are composed of metals like titanium, stainless steel, and their alloys, which provide the necessary strength and support for proper bone healing[9]. These materials are chosen for their biocompatibility and ability to withstand the mechanical demands placed on them during the healing process. Titanium has a Young's modulus five times higher than that of human cortical bone. Because metallic plates are far more rigid than cortical bones, they can transmit higher stresses for bone fixation more efficiently [10], [11].

In real life, the load that a plate places on the tibia depends on several parameters, like the kind of fractures, the position of the plate (medial, anterior-lateral, or posterior medial), the quantity and arrangement of screws, and the material, thickness, and shape of the plate[12]. Small changes to the screw's placement or the position of the plate relative to the bone's surface can have a big influence on the assembly's stability. For the assessment of the tibial bone plate's biomechanical performance in actual clinical stress scenarios [13]. By using FEA software like COMSOL to simulate several mechanical tests like von Mises stress and maximal 1st main stress, it may determine the mechanical strength of a three-dimensional object. In mechanical strength research, von Mises stress is commonly used because it is equal to the effective pressure encountered. Without shear strain, the 1st primary stress displays the greatest (first) and minimum (third) stresses in the normal direction[14]. The initial (highest) primary stress, which indicates an increase in the model's length or thickness, is often positive. Together with total displacement, these two are mostly used in FEM simulations to analyze the mechanical strength of a model[15] .

This research uses a tibia bone that has a 1 mm fracture. The plate is made of Ti and SS alloys, and the fracture is fixed with screws[16]. Five loading scenarios were examined to reflect common physiological loads: compression (axial force), extension (tensile axial force), bending (Y-axis moment), torsion (X-axis torque), and combined load [17], [18]. The current study's findings will yield important information on the tibia bone's mechanical behavior under various stress scenarios. Decisions about surgery and implant design may be based on this information. By accurately reflecting real-world situations, this study advances orthopedic biomechanics and patient care.

2 METHODOLOGY

The mechanical accuracy of a design can be determined using a finite element method (FEM)

or finite element analysis (FEA). FEM, or FEA, allows for the simulation of complex loading conditions on the tibia bone, providing insights into stress distribution and potential failure points[14]. By analyzing these results, researchers can optimize implant designs and surgical techniques for better patient outcomes. FEA is an important step since it removes any extra steps, especially before a prototype is made. In addition to saving time and unnecessary costs, this indicates how strong the model is mechanically[19].

2.1 Finite Element Model Design

The fixation of tibial fractures using two distinct material plates under various physiological settings is the main topic of this research. One of the primary load-bearing bones in the human leg is the tibia. When standing or walking, it transmits loads between the foot and femur[20]. Like other bones, the center of a bone is composed of trabecular bone, while the exterior portion is composed of cortical bone. Hard, thick tissue makes up cortical bone, which is involved in load transfer processes including compression and bending. The trabecular portion, on the other hand, is made of spongy tissue to decrease structural bulk[21].

The tibia bone was demonstrated as a cylindrical hollow to make the geometry easier to understand. The tibia measured 0.3m in overall height, 0.008m in inner radius, and 0.012m in outer radius, according to scientific records. Finite element simulations of the tibia's structural response under various loading conditions and material types were performed using this model. In order to replicate a realistic cortical fracture, a 0.001m crack was created near the tibia bone's center. An oval cross-section perpendicular to the bone's long axis was used to illustrate the crack. The specifications of the plate were 0.12m in length, 0.015m in breadth, and 0.003m in depth. Six screws hold the plate to the tibial bone. In compliance with ordinary implant standards, each screw was constructed as a cylinder with a radius of 0.002m and a length of 0.021m. The screws were placed into the designated holes in the plate to create full contact with the cortical surface of the bone for actual weight transfer [22]. As seen in Fig. 1, COMSOL Multiphysics 6.3 was used to create three-dimensional models.

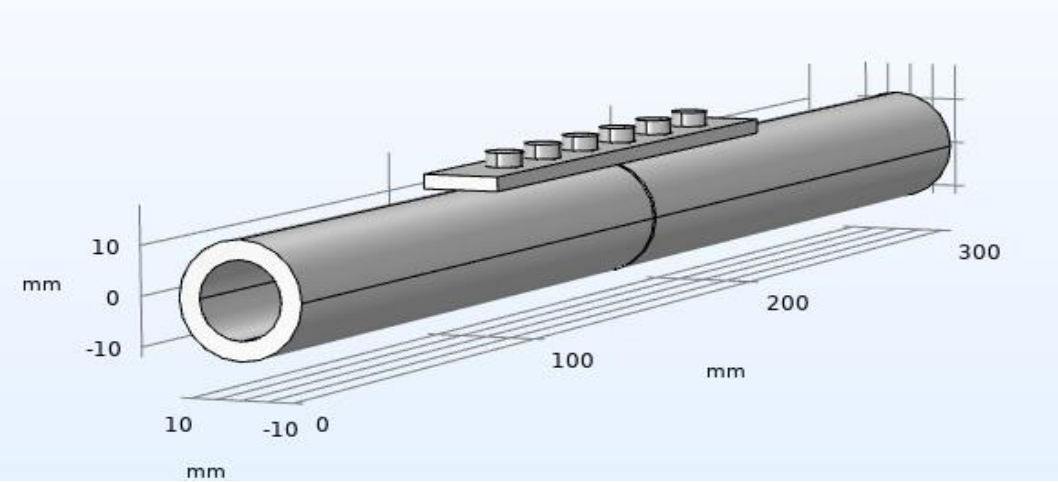

Figure 1:3D design of a tibial bone with plate and screws

2.2 Material Properties

For the tibia bone, choose cortical bone material; for the plate and screws, choose stainless steel and Ti alloy [23], [24], as these materials provide the bone strong strength and are safe under high loads. Table 1 defined the material parameters.

Table 1: Mechanical properties of all materials [25]

Materials	Young's modulus	Poisson's ratio	Density
Cortical	$17x10^9$ Pa	0.3	1900 kg/m³
Titanium alloys	$110x10^9$ Pa	0.34	4430 kg/m³
Stainless Steel 405	$190x10^9$ Pa	0.30	7800 kg/m³

2.3 Meshing and Study

The plate, bone, and screws were surrounded by basic fine mesh in the model. To guarantee the correctness of the answer, mesh convergence investigations were carried out. A stationary solver was used to compute the distribution of stress and deformity due to applied loads.

2.4 FEA Boundary Conditions

Simulations were conducted using COMSOL's solid mechanics module, the bone is subjected to boundary conditions and loads.

As seen in Fig. 2, in Case No. 1, the proximal end of the tibial bone got a fixed support while the distal end experienced a bending force in the XZ plane. This scenario illustrates how the tibia bone bends during a typical walk or when they bend their leg sideways. The distribution of stress throughout the crack site, plate, and screw holes was observed during simulation. A bending moment of M = 15000Nmm was given to the distal end of the tibial bone.

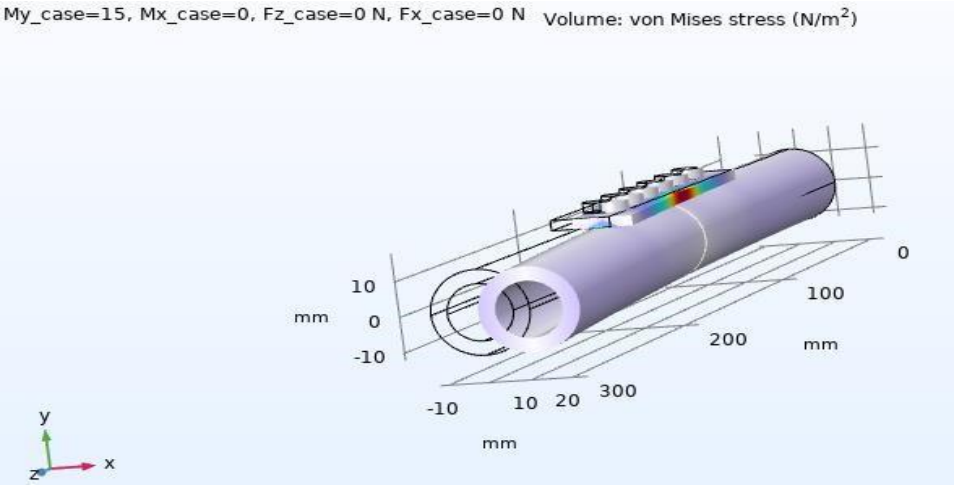

Figure 2: Case 1: distal end of the tibial bone in the XZ plane received a bending force.

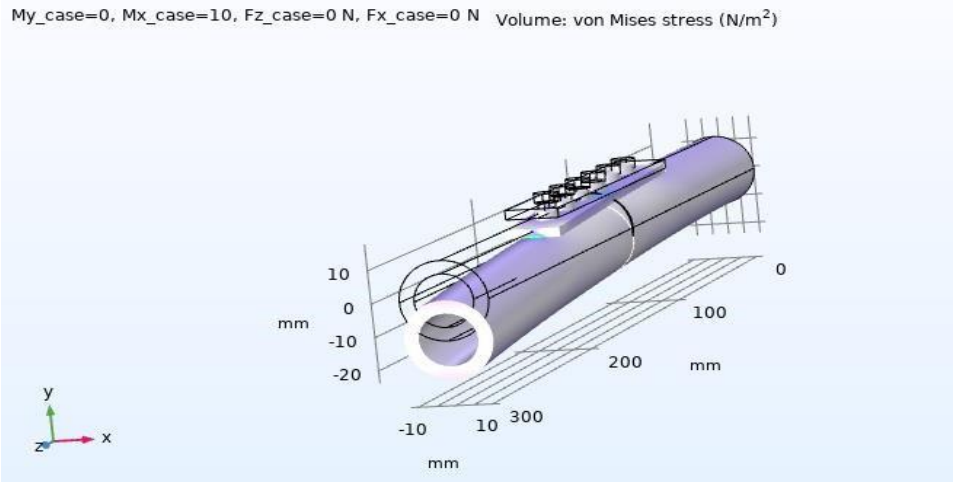

Figure 3:Case 2: distal end of the tibial bone in the YZ plane received a torsional force.

As seen in Fig. 3, in Case No. 2, the proximal end of the tibial bone got a fixed support while the distal end experienced a torsional force in the YZ plane. This scenario illustrates tibial twisting that occurs during activities like abrupt rotations or walking on uneven terrain. Distribute stress equally in the screws, plate, and bone was assessed during the simulation. A torsional moment of M = 10000 Nmm was given to the distal end of the tibial bone.

As seen in Fig. 4, in Case No. 3, the proximal end of the tibial bone got a fixed support while the distal end along the vertical axis got an axial compressive load. This scenario illustrates the stress response that is transmitted to the tibial bone during standing and walking. The distribution of compressive stress at the crack site and a screw hole was measured during the simulation. The tibia bone-plate model's distal side was subjected to a force F = -500 N.

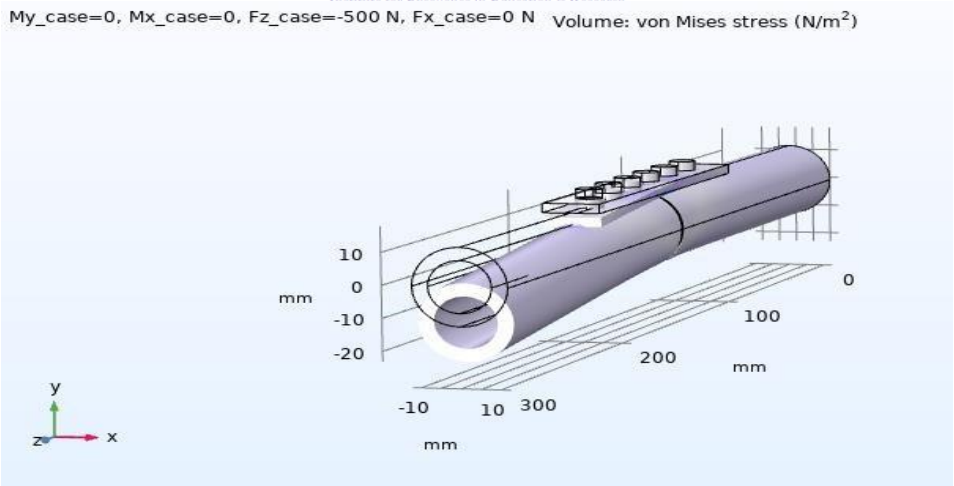

Figure 4:Case 3: distal end of the tibial bone along the vertical axis got an axial compressive force.

As seen in Fig. 5, in Case No. 4, the proximal end of the tibial bone got a fixed support while the distal end along the X-axis experienced an extensive load. This scenario illustrates an extension stress on the tibia. The distribution of tensile stress at the crack site, plate, and within each bone screw hole was obtained throughout the simulation. The tibia bone-plate model's distal side was subjected to a force F = 500N.

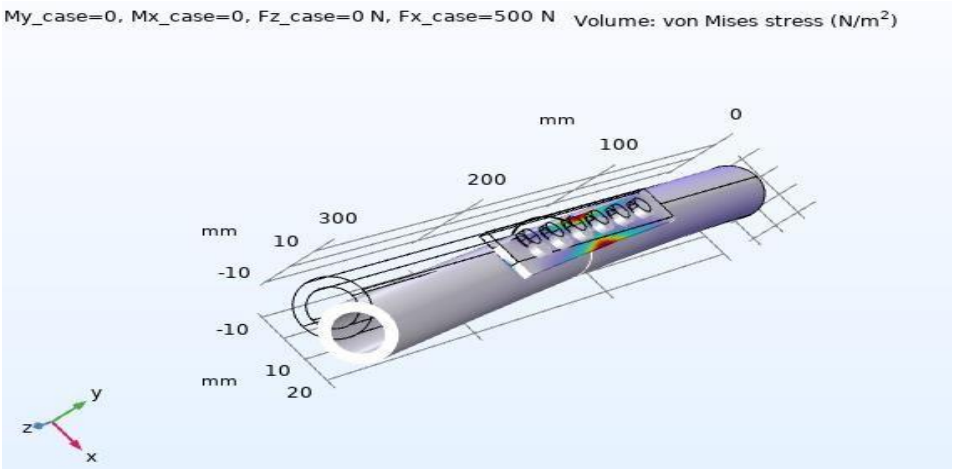

Figure 5:Case 4: distal end of the tibia bone along the X-axis received an extensive force.

As seen in Fig. 6, in Case No. 5, the proximal end of the tibial bone got a fixed support while the distal end of the tibia bone was subjected to a combined mechanical stress that included bending force, torsional force, compressive force, and extensive force. This scenario illustrates a complicated physiological state in which the tibia bone is simultaneously subject to many stresses. The combined impact of every load on the crack site, plate, and each screw hole in the bone was acquired throughout the simulation.

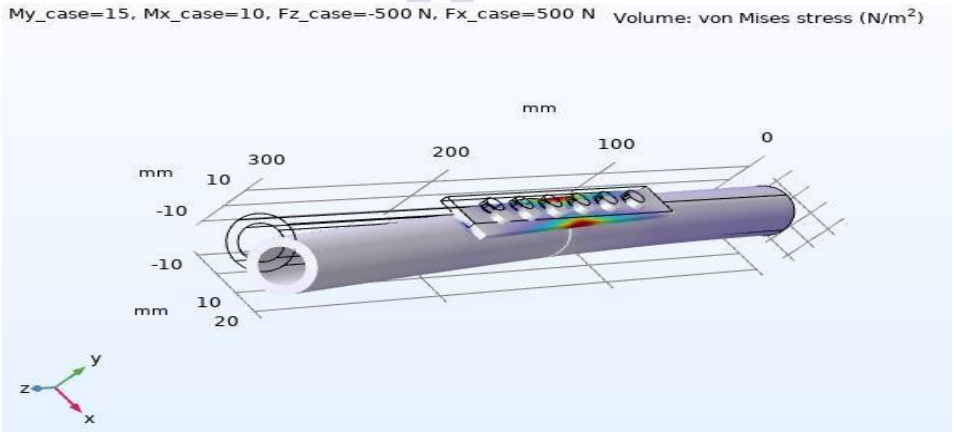

Figure 6:Case 5: Combine mechanical stress

3 RESULTS AND DISCUSSION

The mechanical response of the tibia bone stress analysis model under all five situations is examined using a finite element analysis (FEA) using two distinct materials for the plate and screws. The distribution of stress in the plate, screws, and tibial bone is examined, with a particular emphasis on the bone fracture gap. For both materials, von Mises stress, the first main stress, and total displacement were measured in order to assess all the scenarios.

3.1 Case 1: Bending Moment

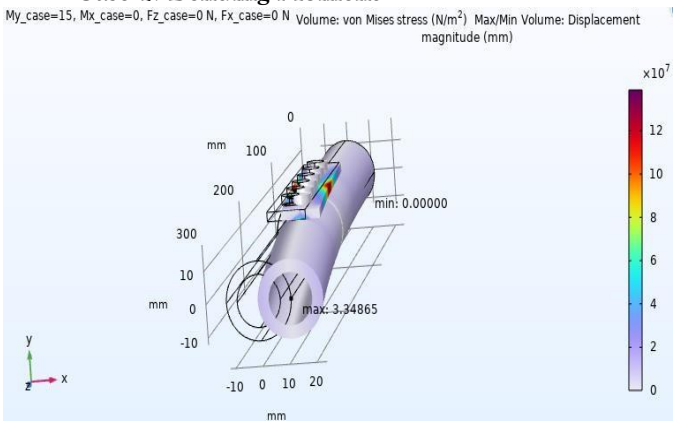

Figure 7: Case 1: 3D displacement in Ti alloy material

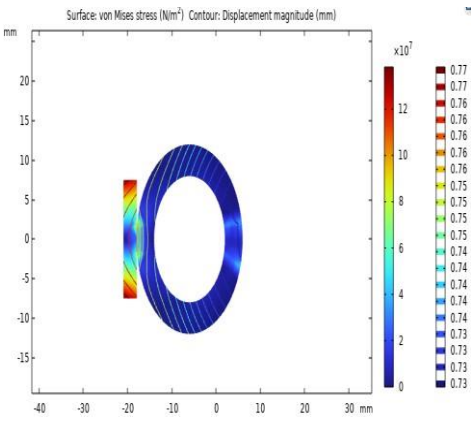

Figure 8: 1D point graph of Ti alloy material

Figure 7 and 8 shows the bending moment condition. In figure 7, displacement ranged from 0 to 3:3486 mm for Ti alloy. Whereas, the figure 8 shows the von mises stress with a peak displacement of 1.4083×10^8 N/m². At the middle of the plate, the 1st primary stress reached its greatest peak at 1.4220×10^8 N/m², indicating a key location of stress concentration. The fact that the deformation was largest near the center of the plate as opposed to the other parts of the bone was further confirmed by the 2D displacement contour figure 9.

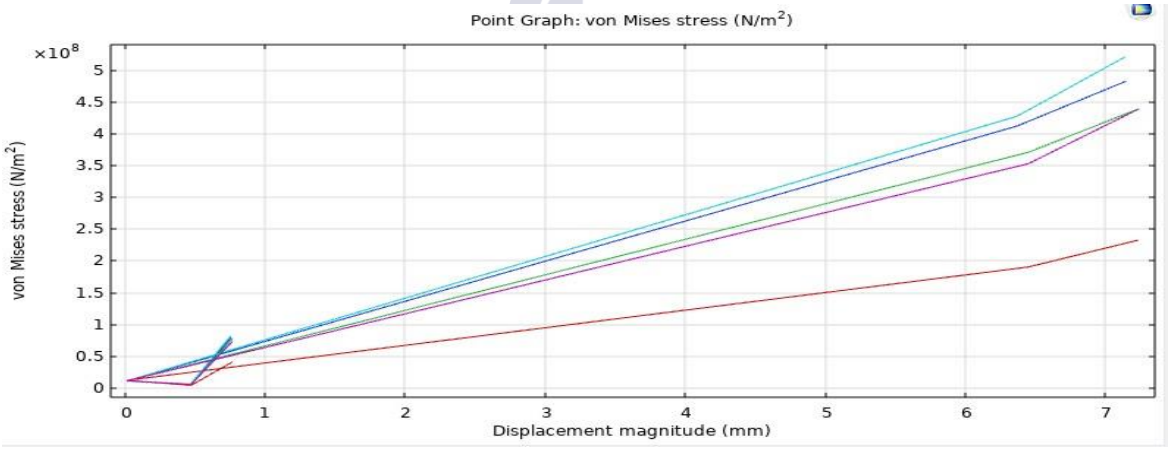

Figure 9: 2D displacement contour

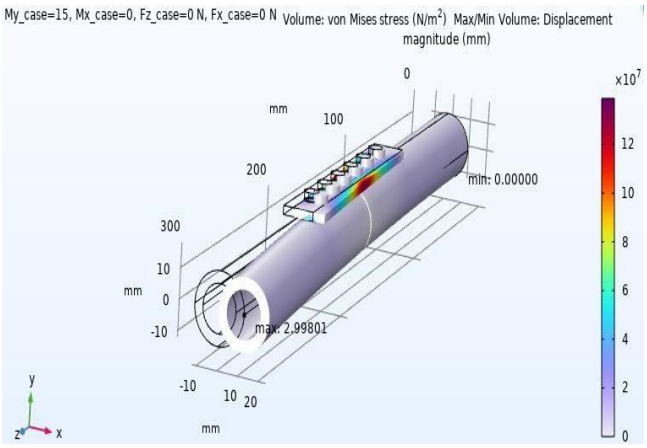

Figure 10: Case 1: 3D displacement in stainless-steel material,

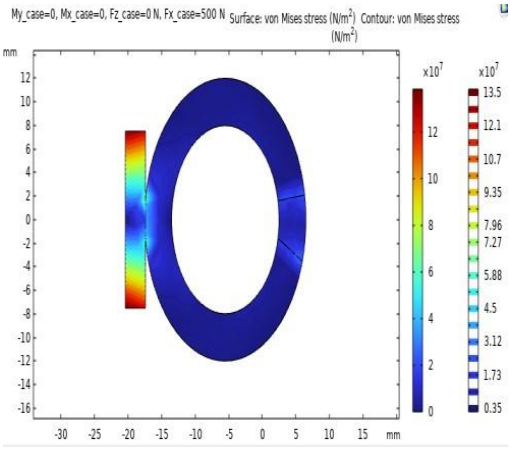

Figure 11: 1D point graph of stainless-steel material

Figure 10 and 11 shows the bending moment condition. In figure 10, displacement ranged from 0 to 2.9980 mm for stainless steel material. Whereas, the figure 11 shows the von mises stress with a peak displacement of 1.4037×10^8 N/m². At the middle of the plate, the 1st primary stress reached its greatest peak at 1.4111×10^8 N/m², indicating a key location of stress concentration. The fact that the deformation was largest near the center of the plate as opposed to the other parts of the bone was further confirmed by the 2D displacement contour figure 12.

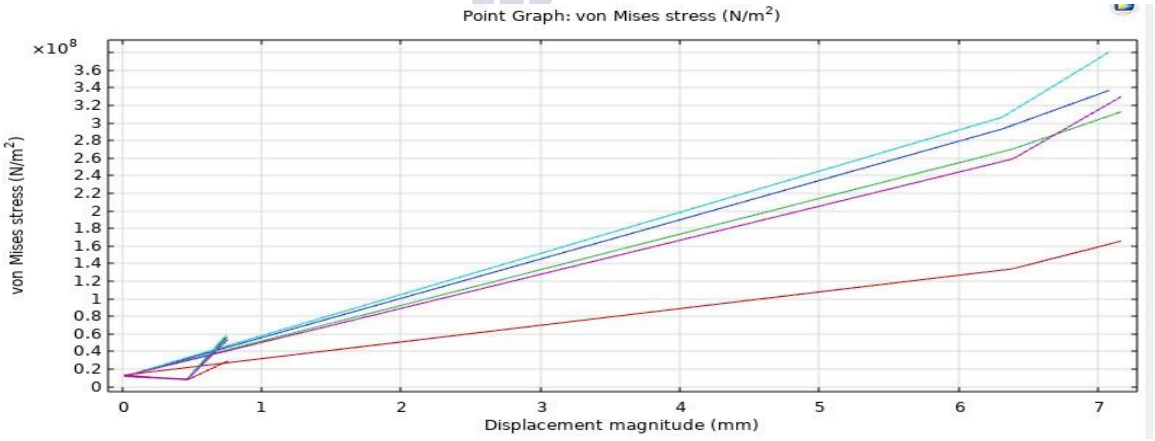

Figure 12: 2D displacement contour

3.2 Case 2: Torsional Moment

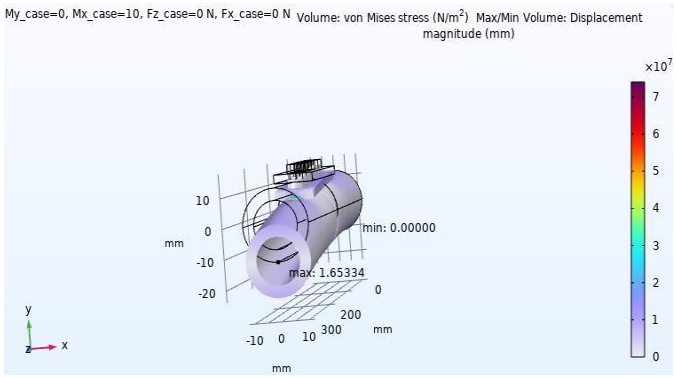

Figure 13: Case 2: 3D displacement in Ti alloy material

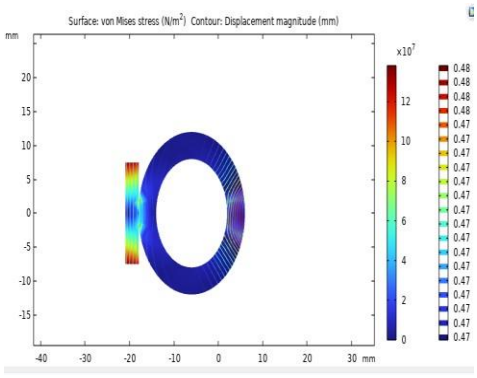

Figure 14: 2D displacement contour

Figure 13 and 8 shows the torsional moment condition. In figure 13, displacement ranged from 0 to 1.6533 mm for Ti alloy. Whereas, the figure 8 shows the von mises stress with a peak displacement of 7.5507×10^7 N/m². At fracture site, the 1st primary stress reached its greatest peak at $8.3711\text{x}10^7$ N/m², indicating a key location of stress concentration. The fact that the deformation was largest near the fracture point as opposed to the other parts of the bone was further confirmed by the 2D displacement contour figure 14.

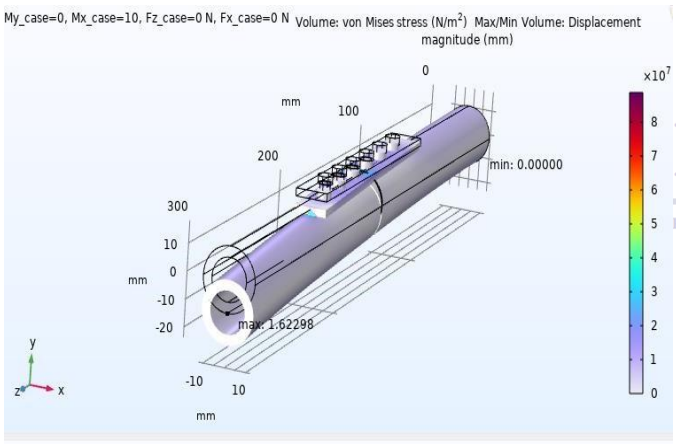

Figure 15: Case 2: 3D displacement in stainless-steel material

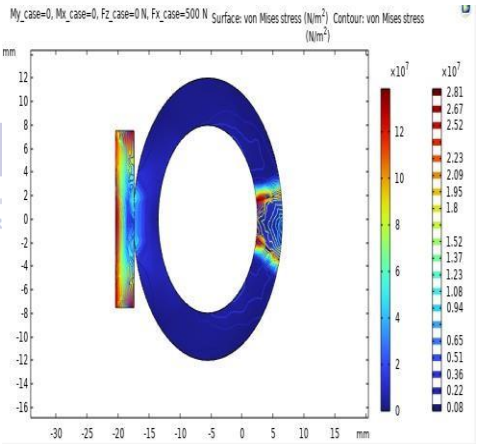

Figure 16: 2D displacement contour

Figure 15 and 11 shows the torsional moment condition. In figure 15, displacement ranged from 0 to 1.6229 mm for stainless steel material. Whereas, the figure 11 shows the von mises stress with a peak displacement of $8.8673\text{x}10^7$ N/m². At fracture site, the 1st primary stress reached its greatest peak at $9.4984\text{x}10^7$ N/m², indicating a key location of stress concentration. The fact that the deformation was largest near the fracture point as opposed to the other parts of the bone was further confirmed by the 2D displacement contour figure 16.

3.3 Case 3: Compression Force

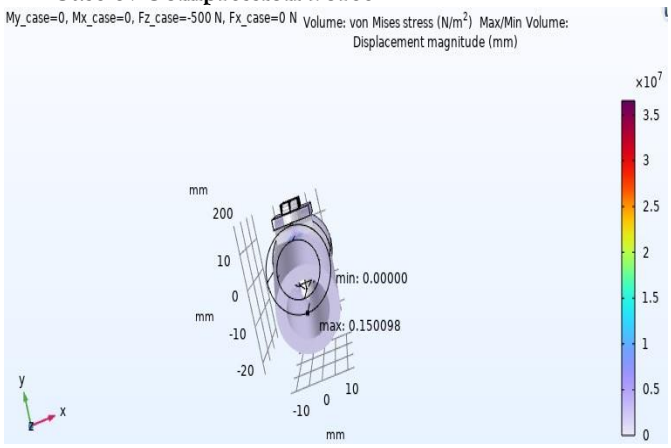

Figure 17: Case 3: 3D displacement in Ti alloy material

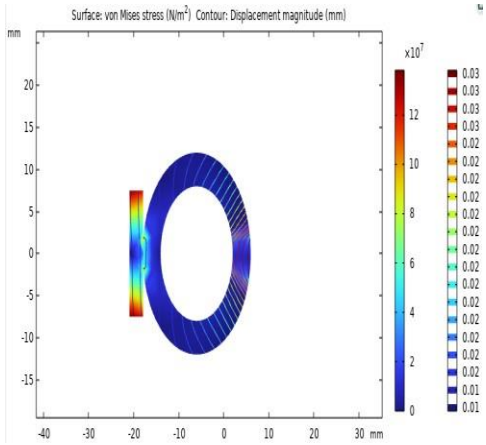

Figure 18: 2D displacement contour

Figure 17 and 8 shows the compression force condition. In figure 17, displacement ranged from 0 to 0.1500 mm for Ti alloy. Whereas, the figure 8 shows the von mises stress with a peak displacement of 3.6546×10^7 N/m². At fracture site, the 1st primary stress reached its greatest peak at 1.0898×10^7 N/m², indicating a key location of stress concentration. The fact that the deformation was largest near the fracture point as opposed to the other parts of the bone was further confirmed by the 2D displacement contour figure 18.

Figure 19 and 11 shows the compression force condition. In figure 19, displacement ranged from 0 to 0.1561 mm for stainless steel material. Whereas, the figure 11 shows the von mises stress with a peak displacement of 3.5606×10^7 N/m². At fracture site, the 1st primary stress reached its greatest peak at 1.1465×10^7 N/m², indicating a key location of stress concentration. The fact that the deformation was largest near the fracture point as opposed to the other parts of the bone was further confirmed by the 2D displacement contour figure 20.

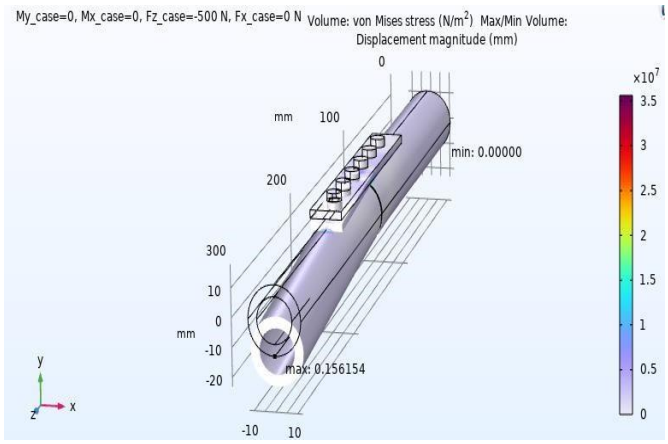

Figure 19: Case 3: 3D displacement in stainless-steel material

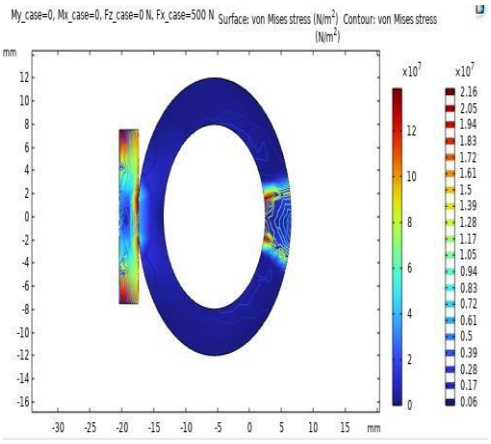

Figure 20: 2D displacement contour

3.4 Case 4: Extension Force

Figure 21 and 8 shows the extension force condition. In figure 21, displacement ranged from 0 to 21.863 mm for Ti alloy. Whereas, the figure 8 shows the von mises stress with a peak displacement of 7.0182×10^8 N/m². At the middle

of the plate sides, the 1st primary stress reached its greatest peak at 7.0978×10^8 N/m^2, indicating a key location of stress concentration. The fact that the deformation was largest near the center of the plate sides as opposed to the other parts of the bone was further confirmed by the 2D displacement contour figure 22.

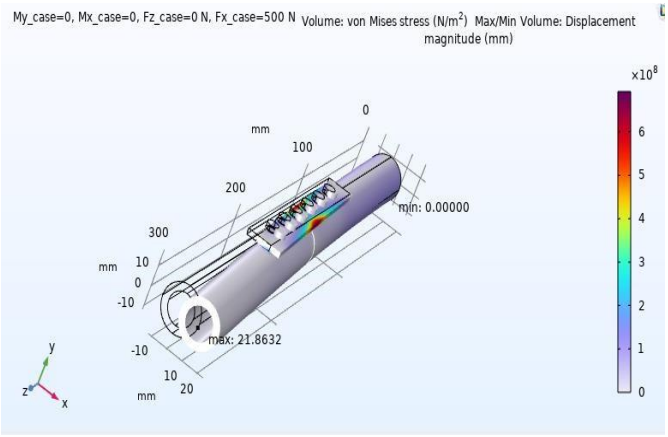

Figure 21: Case 4: 3D displacement in Ti alloy material

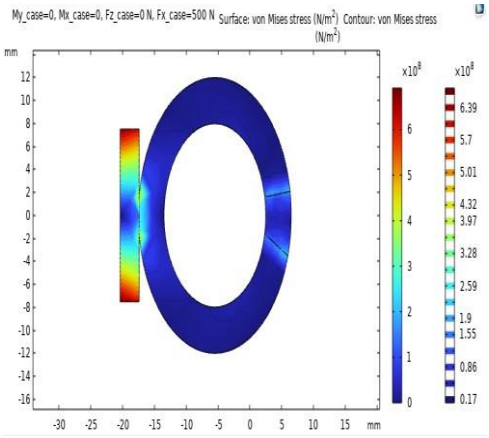

Figure 22: 2D displacement contour

Figure 23 and 11 shows the extension force condition. In figure 23, displacement ranged from 0 to 20.104 mm for stainless steel material. Whereas, the figure 11 shows the von mises stress with a peak displacement of 8.0382×10^8 N/m^2. At the middle of the plate sides, the 1st primary stress reached its greatest peak at 8.1561×10^8 N/m^2, indicating a key location of stress concentration. The fact that the deformation was largest near the center of the plate sides as opposed to the other parts of the bone was further confirmed by the 2D displacement contour figure 24.

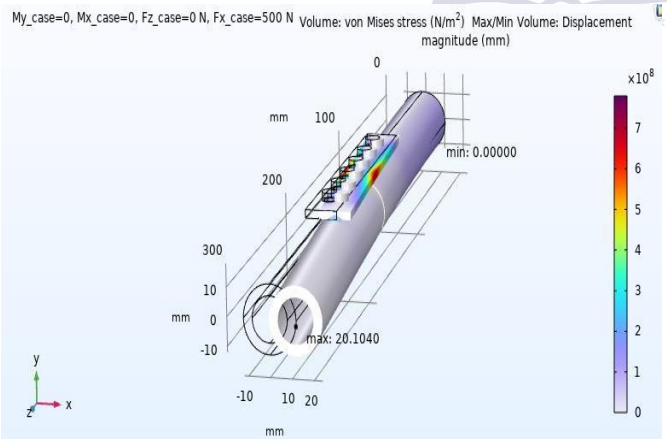

Figure 23: Case 4: 3D displacement in stainless-steel material

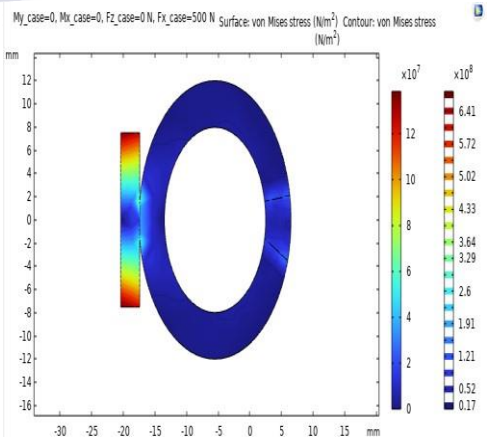

Figure 24: 2D displacement contour

3.5 Case 5: Combined Load

In the combined load condition, the displacement values for the Ti alloy ranged from 0 to 25.299 mm (Fig. 25), mostly focused in the distal portion. Von Mises stress increases gradually with displacement in 1D point graphs, peaking at 8.6975x10^8 N/m^2 (Fig. 11). The critical stress concentration region was indicated by the maximal initial primary stress at the fracture site, which was 8.7629×10^8 N/m^2. Further evidence that the deformation was greatest in the center of the plate sides relative to the rest of the bone was provided by the 2D displacement contour (Fig. 26).

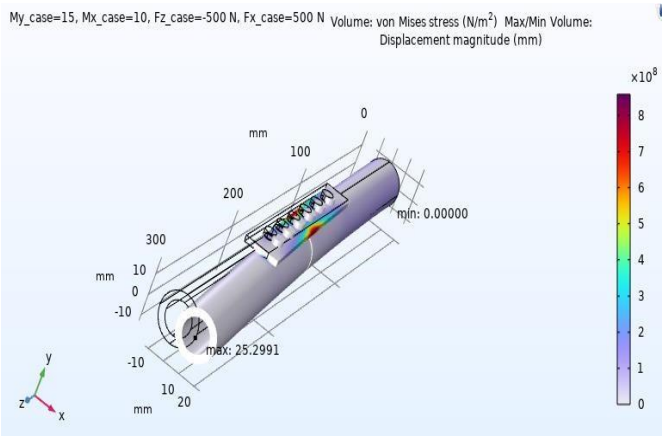

Figure 25: Case 5: 3D displacement in Ti alloy material

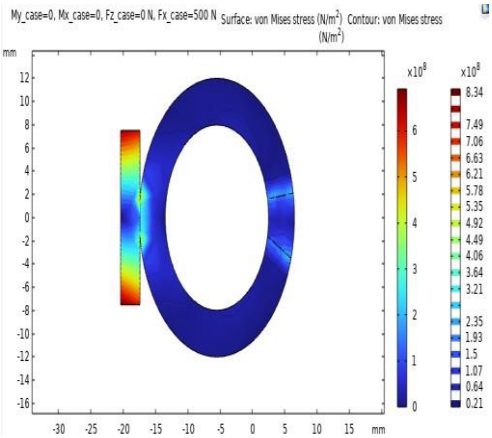

Figure 26: 2D displacement contour

In the combined load condition, the displacement values for the stainless steel material ranged from 0 to 23.186 mm (Fig. 27), mostly focused in the distal portion. Von Mises stress increases gradually with displacement in 1D point graphs, peaking at 9.8428x108 N/m² (Fig. 11). The critical stress concentration region was indicated by the maximal initial primary stress at the fracture site, which was 1.0101×109 N/m². Further evidence that the deformation was greatest in the center of the plate sides relative to the rest of the bone was provided by the 2D displacement contour (Fig. 28).

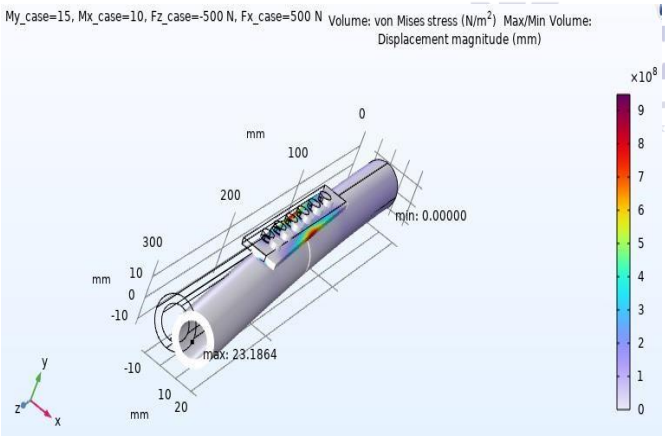

Figure 27: Case 4: 3D displacement in stainless-steel material

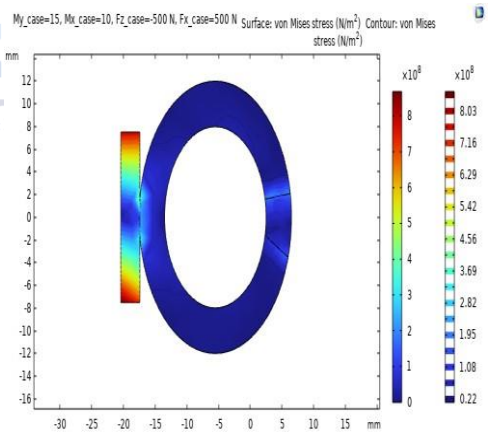

Figure 28: 2D displacement contour

3.6 Summary

This research goal is to determine the mechanical responses of titanium alloy and stainless steel plate and screws in a tibial fracture healing mechanism across a range of physiological stress scenarios. Five different physiological loading situations were modeled using COMSOL: compression force, extension force, bending moment, torsional moment, and combined load. In contrast to the modest deformation and stress levels caused by bending, torsion, compression, and extension, combined loads result in substantial levels of deformation and stress in both materials. Ti alloy exhibits greater deformation under combined load than stainless steel, whereas stainless steel has a higher stress level than Ti alloy.

4 CONCLUSION AND FUTURE WORK

Using COMSOL Multiphysics, the study employed finite element approaches to examine the effects of various physiological states, including bending, torsion, compression, extension, and combined load[13]. Results showed that the titanium alloy Ti-6Al-4V exhibited better performance under combination loading compared to stainless steel, with lower stress concentrations and deformation. This information can be valuable for designing implants or structures that will be subjected to various loading conditions in real-world applications. Additionally, the study highlighted the importance of considering material properties and loading conditions when designing implants for optimal performance. These findings can help improve the durability and reliability of biomedical devices in clinical settings. In the future, it is advised to evaluate the effects of other materials, such as carbon fiber, etc., and investigate how different materials affect bone-plate fixation under different physiological conditions.

REFERENCES

[1] F. C. M. Driessens, "Probable Phase Composition of the Mineral in Bone," 1980.

[2] K. A. Athanasiou, C.-F. Zhu, D. R. Lanctot, C. M. Agrawal, and X. Wang, "Fundamentals of Biomechanics in Tissue Engineering of Bone," Tissue Eng., vol. 6, no. 4, pp. 361–381, Aug. 2000, doi: 10.1089/107632700418083.

[3] M. J. Yaszemski, R. G. Payne, W. C. Hayes, R. Langer, and A. G. Mikos, "Evolution of bone transplantation: molecular, cellular and tissue strategies to engineer human bone," Biomaterials, vol. 17, no. 2, pp. 175–185, Jan. 1996, doi: 10.1016/0142-9612(96)85762-0.

[4] J. Tan et al., "Effects of bone-plate materials on the healing process of fractured tibia bone under time-varying conditions: a finite element analysis," Mater. Res. Express, vol. 8, no. 9, p. 095308, Sep. 2021, doi: 10.1088/2053-1591/ac24f8.

[5] L. Tamburini et al., "A Review of Tibial Shaft Fracture Fixation Methods," Trauma Care, vol. 3, no. 3, pp. 202–211, Sep. 2023, doi: 10.3390/traumacare3030019.

[6] J. Kurniawan, S. Y. Lin, and W. T. Wang, "Development and Finite Element Analysis of a Novel Bent Bone Plate," Applied Sciences (Switzerland), vol. 12, no. 21, Nov. 2022, doi: 10.3390/app122110900.

[7] Z.-W. Duan and H. Lu, "Effect of Mechanical Strain on Cells Involved in Fracture Healing.," Orthop. Surg., vol. 13, no. 2, pp. 369–375, Apr. 2021, doi: 10.1111/os.12885.

[8] S. M. Perren, "Physical and biological aspects of fracture healing with special reference to internal fixation.," Clin. Orthop. Relat. Res., no. 138, pp. 175–96, 1979.

[9] J. R. Sheen, A. Mabrouk, and V. V. Garla, Fracture Healing Overview. 2025.

[10] A. A. Al-Tamimi, P. R. A. Fernandes, C. Peach, G. Cooper, C. Diver, and P. J. Bartolo, "Metallic bone fixation implants: a novel design approach for reducing the stress shielding phenomenon," Virtual Phys. Prototyp., vol. 12, no. 2, pp. 141–151, Apr. 2017, doi: 10.1080/17452759.2017.1307769.

[11] C. C. Barber, M. Burnham, O. Ojameruaye, and M. D. McKee, "A systematic review of the use of titanium versus stainless steel implants for fracture fixation," OTA Int., vol. 4, no. 3, p. e138, Sep. 2021, doi: 10.1097/OI9.0000000000000138.

[12] J. Kurniawan, S. Y. Lin, and W. T. Wang, "Development and Finite Element Analysis of a Novel Bent Bone Plate," Applied Sciences (Switzerland), vol. 12, no. 21, Nov. 2022, doi: 10.3390/app122110900.

[13] K. R. Zhang et al., "A finite element study for tibial fractures: analyze the biomechanical condition of the tibial fracture area to provide guidance for subsequent treatment," Front. Bioeng. Biotechnol., vol. 13, 2025, doi: 10.3389/fbioe.2025.1532207.

[14] N. Özgun, M. Sc Dipl Wi-Ing Michael Busse, M. Sc Ing Ernesto González Trejo, and M. Sc, "Finite Element Method (FEM) & COMSOL A (very) brief introduction," 2013.

[15] A. Şoica, S. Apostu, and C. Pupaza, "Design and Simulation of Mechanical Structures Using FEM (Finite Element Method)," Journal of Research and Innovation for Sustainable Society, vol. 7, no. 1, pp. 126–131, Mar. 2025, doi: 10.33727/JRISS.2025.1.11:126-131.

[16] F. D. Al-Shalawi et al., "Biomaterials as Implants in the Orthopedic Field for Regenerative Medicine: Metal versus Synthetic Polymers," Polymers (Basel)., vol. 15, no. 12, p. 2601, Jun. 2023, doi: 10.3390/polym15122601.

[17] A. A. Al-Tamimi, C. Quental, J. Folgado, C. Peach, and P. Bartolo, "Stress analysis in a bone fracture fixed with topology-optimised plates," Biomech. Model. Mechanobiol., vol. 19, no. 2, pp. 693–699, Apr. 2020, doi: 10.1007/s10237-019-01240-3.

[18] M. Palka, P. Miszczyk, M. Jurewicz, and R. Perz, "Finite element method analysis of bone stress for variants of locking plate placement," Heliyon, vol. 10, no. 8, Apr. 2024, doi: 10.1016/j.heliyon.2024.e26840.

[19] H. Ahirwar, V. K. Gupta, and H. S. Nanda, "Finite element analysis of fixed bone plates over fractured femur model," Comput. Methods Biomech. Biomed. Engin., vol. 24, no. 15, pp. 1742–1751, 2021, doi: 10.1080/10255842.2021.1918123.

[20] R. Zdero, K. Gide, P. Brzozowski, E. H. Schemitsch, and Z. S. Bagheri, "Biomechanical design optimization of distal femur locked plates: A review," Proc. Inst. Mech. Eng. H, vol. 237, no. 7, pp. 791–805, Jul. 2023, doi: 10.1177/09544119231181487.

[21] S.-H. Kim, S.-H. Chang, and H.-J. Jung, "The finite element analysis of a fractured tibia applied by composite bone plates considering contact conditions and time-varying properties of curing tissues," Compos. Struct., vol. 92, no. 9, pp. 2109–2118, Aug. 2010, doi: 10.1016/j.compstruct.2009.09.051.

[22] M. Ceddia, G. Solarino, M. Tucci, L. Lamberti, and B. Trentadue, "Stress Analysis of Tibial Bone Using Three Different Materials for Bone Fixation Plates," Journal of Composites Science, vol. 8, no. 9, Sep. 2024, doi: 10.3390/jcs8090334.

[23] S. Benli, S. Aksoy, H. Havıtcıoğlu, and M. Kucuk, "Evaluation of bone plate with low-stiffness material in terms of stress distribution," J. Biomech., vol. 41, no. 15, pp. 3229–3235, Nov. 2008, doi: 10.1016/j.jbiomech.2008.08.003.

[24] W. Abd-Elaziem, M. A. Darwish, A. Hamada, and W. M. Daoush, "Titanium-Based alloys and composites for orthopedic implants Applications: A comprehensive review," Mater. Des., vol. 241, p. 112850, May 2024, doi: 10.1016/j.matdes.2024.112850.

[25] N. Fouda, R. Mostafa, and A. Saker, "Numerical study of stress shielding reduction at fractured bone using metallic and composite bone-plate models," Ain Shams Engineering Journal, vol. 10, no. 3, pp. 481–488, Sep. 2019, doi: 10.1016/j.asej.2018.12.005.